

Steady and Time-Resolved Photoelectron Spectra Based on Nuclear Ensembles

Wilmer Arbelo-González,[†] Rachel Crespo-Otero,[‡] and Mario Barbatti^{*,†,§}

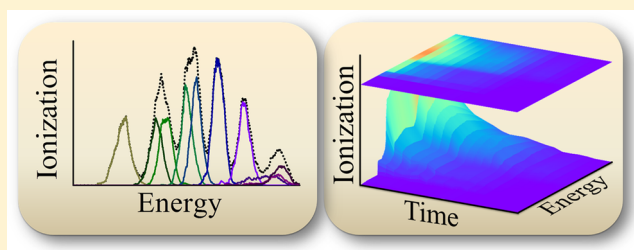
[†]Max-Planck-Institut für Kohlenforschung, Kaizer-Wilhelm-Platz 1, 45470 Mülheim an der Ruhr, Germany

[‡]School of Biological and Chemical Sciences, Queen Mary University of London, Mile End Road, London E1 4NS, United Kingdom

[§]Aix Marseille Université, CNRS, ICR, Marseille, 13284, France

Supporting Information

ABSTRACT: Semiclassical methods to simulate both steady and time-resolved photoelectron spectra are presented. These approaches provide spectra with absolute band shapes and vibrational broadening beyond the Condon approximation, using an ensemble of nuclear configurations built either via distribution samplings or nonadiabatic dynamics simulations. Two models to account for the electron kinetic energy modulation due to vibrational overlaps between initial and final states are discussed. As illustrative examples, the steady photoelectron spectra of imidazole and adenine and the time- and kinetic-energy-resolved photoelectron spectrum of imidazole were simulated within the frame of time-dependent density functional theory. While for steady spectra only electrons ejected with maximum allowed kinetic energy need to be considered, it is shown that to properly describe time-resolved spectra, electrons ejected with low kinetic energies must be considered in the simulations as well. The results also show that simulations based either on full computation of photoelectron cross section or on simple Dyson orbital norms provide results of similar quality.



1. INTRODUCTION

To provide results directly comparable to experimental data is a major goal in computational theoretical chemistry. This goal represents a special challenge with the natural trend of dealing with always larger and more complex molecular systems. Whenever nonlocal quantum effects can be neglected, resorting to semiclassical simulations turns out to be a good option, as it allows closely emulating experimental techniques at relatively modest computational costs compared to full quantum simulations.

In the last years, within the development of the NEWTON-X platform,^{1,2} we have worked out and implemented diverse semiclassical approaches for dynamics and spectrum simulations. A central point in these developments has been the extensive use of population sampling via nuclear ensembles.^{3,4} In the present work, this approach will once more play an important role for the implementation of semiclassical methods for simulations of steady and time-resolved photoelectron (PE) spectra.

The nuclear ensemble approach can be understood as a technique to recover inhomogeneous broadening dating back to the works of Kubo,⁵ and of Wilson and Heller,⁶ among others. It is likely the simplest method to obtain absolute spectral bands. It works in three steps: (i) an ensemble of nuclear geometries is built to represent the vibrational distribution in the source state; (ii) spectral intensities between the source and the target states are computed for each point in the ensemble; (iii) the final spectrum is obtained as an

incoherent sum over all these individual transitions. Thus, the vibrational features of the spectrum are first supposed to be essentially dependent on source–state nuclear wave function and any property depending on the correlation between the source and target nuclear wave functions is neglected (vibrational structures in the electronic spectrum, for instance).

Nuclear ensembles have been chiefly used to simulate steady electronic spectra and to sample initial conditions for dynamics simulations. Going beyond its very intuitive background, we have shown in ref 3 how the nuclear ensemble approach is correlated to more formal methods. Recently, Bennett and co-workers,⁷ presented the approach as a particular case of a unified description of time-resolved spectroscopies. Also, Petit and Subtonik⁸ have developed ensemble-based methods for recovering source/target correlation. The impact on the spectrum and dynamics results due to different ways of building the ensemble has been discussed in refs 4 and 9.

The nuclear ensemble approach has been applied for simulations of different types of time-resolved spectra, including two-dimensional,¹⁰ stimulated emission,¹¹ photoelectron,^{7,12–17} ultrafast Auger,^{7,18} and X-ray photoscattering⁷ spectroscopies. These developments have been based on a broad range of approximations and electronic structure methods, from very simple estimates of transition probabilities^{7,14,15,19–22} to more involved modeling with full computation of transition mo-

Received: July 14, 2016

75 ments.^{13,16,17,21,23,24} Here, we present a new implementation of
 76 the method aiming at photoelectron spectroscopy, which,
 77 although it shares a number of common features with previous
 78 implementations (especially those reported in refs 7 and 19),
 79 distinguishes itself by its generality; allowing simulations of
 80 steady and time-resolved spectra, use of arbitrary ensembles,
 81 investigation of general molecular systems, control of diverse
 82 parameters, choice of particular models for intensity calculation
 83 and vibrational overlap modulation, direct integration with any
 84 electronic structure method, and computation of intensities
 85 with absolute units. To simulate steady and time-resolved
 86 photoelectron spectra we should consider three different
 87 aspects: computation of ionization energies, computation of
 88 ionization probabilities, and how to put these results together
 89 to build the spectrum.

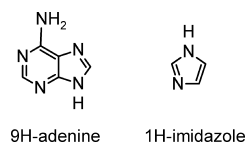
90 Over the years, computations of ionization energies have
 91 developed through two orthogonal methodological branches.
 92 On the one hand, there are a large number of methods based
 93 on quasi-particle methods, where many-body effects on
 94 Koopmans ionization are perturbatively recovered,^{25–28} as in
 95 the popular outer-valence Green's function method.^{26,28} In this
 96 context, Koopmans-compliant functionals have shown promis-
 97 ing results for the simulation of photoelectron spectra as well.²⁹
 98 On the other hand, ionization energies have also been
 99 simulated based on the difference between independent
 100 calculations for the N and $N - 1$ electron systems, the so-
 101 called Δ approach.³⁰ The Δ approach has been regarded as less
 102 accurate than the former, especially within the Δ_{SCF}
 103 approximation, based on the difference between Hartree-
 104 Fock energies and wave functions. However, with the
 105 development of new and more accurate methods for excited
 106 state calculations, a proper balance between the estimates for
 107 the N and $N - 1$ electron systems could be achieved, and
 108 methods as Δ_{CASPT2} , Δ_{CC2} , and Δ_{TDDFT} may provide accurate
 109 (within 0.2 eV) photoelectron information.³¹ In view of the
 110 flexibility of the Δ methods to be systematically applied to a
 111 large number of points in the ensemble, we have based our
 112 current developments on them, even though we had to pay the
 113 price of dealing with nonorthogonal sets of orbitals for
 114 computation of intensities, as discussed later.

115 Computation of ionization probabilities have a long history
 116 dating back several decades.^{32–35} These calculations are not of
 117 our direct concern here. Instead, we have used a third-party
 118 program^{34,36} to compute ionization cross sections using
 119 standard methods, as explained below. However, for using
 120 these methods, Dyson orbitals are needed, and their
 121 computation within TDDFT frame is also discussed below.

122 Lastly, having computed ionization energies and probabili-
 123 ties, we must put them together in a spectral representation. In
 124 the present work, we do this using the nuclear ensemble
 125 approach. Formal quantum approaches for steady and time-
 126 resolved photoelectron spectrum simulations of molecules have
 127 also been available for many years,^{7,25,35,37} and their success is
 128 well documented.^{7,38–42} Thus, the approach presented here
 129 must not be understood as a new theory aimed at replacing the
 130 previous ones. Instead, it should be taken as a routine approach,
 131 especially useful in the context of a trajectory-based dynamics
 132 simulations for large molecules, where ensembles are automati-
 133 cally generated and must be analyzed. We, yet, emphasize that
 134 the nuclear ensemble is a low-resolution semiclassical approach.
 135 It cannot be expected to compete with formal quantum
 136 methods, which are obviously the most indicated option for
 137 problems requiring high accuracy.

We will demonstrate here the potential applications and
 138 caveats of the nuclear ensemble approach for photoelectron
 139 spectroscopy with simulations of the steady PE spectra of
 140 adenine and imidazole (Scheme 1) and the time-resolved PE
 141 s1

Scheme 1



spectrum of imidazole, always in the gas phase. The choice of
 142 these systems followed a pragmatic logic: first experimental and
 143 computational data are available for comparison;^{43–51} and
 144 second we have previously studied the photoelectron spectro-
 145 scopy of both systems,^{15,31,52} which will spare us of discussing
 146 their very interesting photophysics this time to primarily focus
 147 on the method implementation itself.
 148

Finally, we should add that all developments discussed here
 149 have been implemented in NEWTON-X and are available in the
 150 new versions of the program.
 151

2. THEORY

2.1. Steady PE Spectra. Consider the photoionization
 152 process depicted in Figure 1. A N -electrons molecule in the
 153 s1

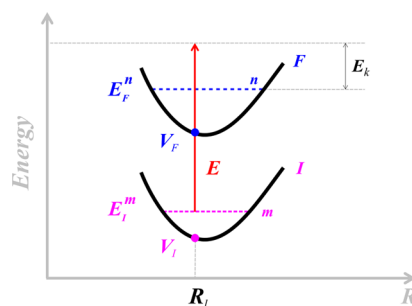


Figure 1. Schematic representation of the photoionization for the steady case.

electronic state I and the stationary vibrational level m , with
 154 eigenvalue E_I^m , is excited with a monochromatic laser of fixed
 155 energy E . As a result, an electron with asymptotic kinetic energy
 156 $E_k = \hbar^2 k^2 / 2m_e$ (m_e and k are the mass and wavevector of the
 157 photoelectron) is ejected, leaving the remaining $N - 1$ electron
 158 system in the electronic state F and vibrational level n , with
 159 eigenvalue E_F^n .
 160

From a semiclassical standpoint, the probability of
 161 occurrence of such a process is proportional to the cross
 162 section per unit of electron kinetic energy:
 163

$$\Gamma(E, E_k) = \sum_F \int d\mathbf{R} \rho_{Im}(\mathbf{R}) \sigma_{IF}(E, E_k, \mathbf{R}) \delta(E_k - E + \Delta V_{IF}(\mathbf{R}) + \Delta K_{mn}(\mathbf{R})) \quad (1)$$

where ρ_{Im} is the probability distribution of nuclear coordinates
 165 \mathbf{R} for the source state $|I, m\rangle$, σ_{IF} is the photoionization cross
 166 section between I and F , and the delta function imposes the
 167 energy resonance condition involving the ionization potential
 168 $\Delta V_{IF} = V_F - V_I$ and the kinetic energy difference $\Delta K_{mn} = E_n -$
 169 E_m between the two states. The sum runs over all target F states
 170 contributing to the process.
 171

172 Supposing that the photoprocess is instantaneous and that
 173 the nuclear momentum does not change, $\Delta K_{mn} \approx 0$.
 174 Additionally, replacing the $\delta(x)$ function by a sharp function,
 175 one obtains

$$\Gamma(E, E_k) \approx \sum_F \int d\mathbf{R} \rho_{Im}(\mathbf{R}) \sigma_{IF}(E, E_k, \mathbf{R}) w_s$$

$$[E_k, E - \Delta V_{IF}(\mathbf{R}), \varepsilon] \quad (2)$$

176 where w_s is given either as a normalized Gaussian

$$w_s[E_k, E - \Delta V_{IF}, \varepsilon] = \begin{cases} \frac{1}{(2\pi)^{1/2}(\varepsilon/2)} \exp\left(-\frac{(E_k - (E - \Delta V_{IF}))^2}{2(\varepsilon/2)^2}\right) & \text{for } E_k \leq E - \Delta V_{IF} \\ 0 & \text{for } E_k > E - \Delta V_{IF} \end{cases} \quad (3)$$

178 or a normalized Lorentzian

$$w_s[E_k, E - \Delta V_{IF}, \varepsilon] = \begin{cases} \frac{1}{\pi(\varepsilon/2)} \frac{(\varepsilon/2)^2}{(E_k - (E - \Delta V_{IF}))^2 + (\varepsilon/2)^2} & \text{for } E_k \leq E - \Delta V_{IF} \\ 0 & \text{for } E_k > E - \Delta V_{IF} \end{cases} \quad (4)$$

180 In both cases, ε is an arbitrary parameter determining the line
 181 width. It should be much smaller than the bandwidth to not
 182 interfere with the results, usually $\varepsilon \ll 1$ eV is enough to satisfy
 183 this requirement.

185 2.1.1. Nuclear Ensemble Approach for Steady Spectra.

186 The integral over \mathbf{R} in eq 2 can be solved by a Monte Carlo
 187 procedure, leading to

$$\Gamma(E, E_k) = \sum_F \frac{1}{N_p} \sum_{l=1}^{N_p} \sigma_{IF}(E, E_k, \mathbf{R}_l) w_s$$

$$[E_k, E - \Delta V_{IF}(\mathbf{R}_l), \varepsilon] \quad (5)$$

189 where a set of N_p nuclear geometries \mathbf{R}_l are generated according
 190 to the ρ_{Im} distribution.

191 In the particular case when the system is prepared before the
 192 ionization in the electronic and vibrational ground states $I = 0$
 193 and $m = 0$, it is fair to assume that the harmonic approximation
 194 is valid. Under these conditions, it is more natural,⁴ as well as
 195 numerically efficient, to perform the sampling of the nuclear
 196 configurations in the normal mode coordinates \mathbf{q} , where the
 197 nuclear ensemble is defined by the marginal Wigner
 198 distribution function for the quantum harmonic oscillator⁵³

$$\rho_{00}(\mathbf{q}) = \prod_{i=1}^{N_d} \left(\frac{\mu_i \omega_i}{\pi \hbar} \right)^{1/2} \exp\left(-\frac{\mu_i \omega_i q_i^2}{\hbar} \right) \quad (6)$$

200 Here, ω_i is the angular frequency associated with the i th normal
 201 mode with reduced mass μ_i . N_d is the number of normal modes
 202 in the system. Once N_p nuclear geometries \mathbf{q}_l are generated
 203 according to $\rho_0(\mathbf{q})$, they are transformed back to Cartesian
 204 coordinates \mathbf{R}_l .

205 **2.2. Time-Resolved PE Spectra.** Suppose now that the
 206 molecule is at time $t = 0$ in the electronic and vibrational
 207 ground state, with energy E_0 , when a laser of energy E_1 pumps
 208 it to the excited state I' . This first excitation is considered fully
 209 vertical, so that the nuclear coordinates and conjugate momenta

remain constant. Once in the I' state, the system is allowed to
 evolve freely and, at $t = \tau$, the dynamics is probed by ionizing
 the molecule with a second laser of energy E_2 , exactly under the
 same conditions as in section 2.1. As nonadiabatic transitions
 are allowed during the dynamics, the electronic state I at the
 moment of the ionization, with total energy $E_I = E_0 + E_1$, may
 in general be different of I' . This is schematically depicted in
 Figure 2.

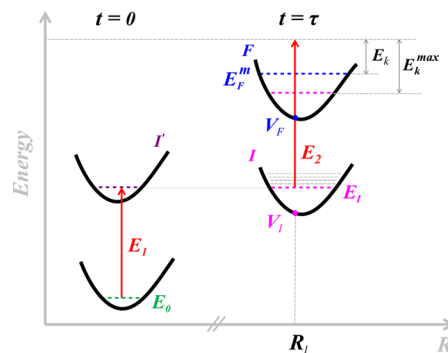


Figure 2. Schematic representation of the photoionization for the time-resolved case.

Given the equivalence, the analysis of this time-resolved
 situation parallels the development of the steady case,
 considering that the effects of the two laser pulses are
 uncorrelated. Nevertheless, there are some fundamental
 differences: first, the nuclear state of the molecule at $t = \tau$
 is described by a wavepacket, not by a single stationary state;
 second, the laser pulse duration is in the femtosecond scale,
 impacting the energy resolution.

Bennett et al.⁷ have shown that the time-resolved case can
 still be written analogously to eq 5, but with the initial ensemble
 distribution given by the population ρ_I^t of state I at time τ . The
 photoelectron spectrum is then given by

$$\Gamma(E_2, E_k, \tau) = \sum_F \int d\mathbf{R} \rho_I^t(\mathbf{R}(\tau)) \sigma_{IF}(E_2, E_k, \mathbf{R}(\tau)) w_s$$

$$[E_k, E_2 - \Delta V_{IF}(\mathbf{R}), \varepsilon] \quad (7)$$

This approximation, which like in the steady case still assumes
 that the nuclear momentum does not change, implies that the
 electron is always ejected with the maximum allowed kinetic
 energy, $E_{k,IF}^{\max} = E_2 - \Delta V_{IF}$.

Because the molecule at time τ is described by a wavepacket
 rather than by a stationary eigenvector of state I , the Franck–
 Condon overlaps between I and F are much more complex
 than in the steady case.³⁹ Therefore, to assume that the nuclear
 momentum remains constant during the phototransition ($E_{k,IF}^{\max}$
 ejection) may be too restrictive. To go beyond this hypothesis,
 we have also tested a model that simply assumes that any value
 between $E_{k,IF}^{\max}$ and $E_k^{\min} = 0$ is equally probable (from the
 vibrational point of view). In this case, the w_s function in eq 7
 should be replaced by a normalized rectangular function
 allowing for contribution in the whole domain:

$$w_r[E_k, E_2 - \Delta V_{IF}] = \begin{cases} (E_2 - \Delta V_{IF})^{-1} & \text{for } E_k \leq E_2 - \Delta V_{IF} \\ 0 & \text{for } E_k > E_2 - \Delta V_{IF} \end{cases} \quad (8)$$

247 With this new assumption, which has also been applied by Fuji
248 et al.,¹⁹ the semiclassical expression for the time-resolved
249 spectrum is

$$\Gamma(E_2, E_k, \tau) = \sum_F \int d\mathbf{R} \rho_1^\tau(\mathbf{R}(\tau)) \sigma_{IF}(E_2, E_k, \mathbf{R}(\tau)) w_r$$

$$[E_k, E_2 - \Delta V_{IF}(\mathbf{R})] \quad (9)$$

251 In the remaining paper, when using sharp w_s functions, we
252 will refer to it as the peaked vibrational background (PVB)
253 model; when using rectangular w_r functions, we will refer to it
254 as the constant vibrational background (CVB) model.

255 **2.2.1. Nuclear Ensemble Approach for Time-Resolved**
256 **Spectra.** Either with eq 7 or with eq 9, the integral over \mathbf{R} is
257 solved by a Monte Carlo procedure, leading to

$$\Gamma(E, E_k, \tau) = \sum_F \frac{1}{N_p} \sum_{l=1}^{N_p} \sigma_{IF}(E, E_k, \mathbf{R}_l(\tau)) w$$

$$[E_k, E - \Delta V_{IF}(\mathbf{R}_l(\tau))] \quad (10)$$

259 where a set of N_p nuclear geometries \mathbf{R}_l are generated according
260 to the ρ_1^τ distribution.

261 In practical terms, the nuclear ensemble $\rho_1^\tau(\mathbf{R})$ at time $t = \tau$ is
262 built by first running a conventional surface hopping
263 simulation,⁵⁴ and then collecting geometries \mathbf{R} within a time
264 window $\tau \leq t < \tau + \Delta\tau$ after the photoexcitation. For each \mathbf{R} ,
265 σ_{IF} is computed for $E_{k,IF}^{\max}$ in the case of eq 7 or for n_i values of E_k
266 regularly spaced between zero and $E_2 - \Delta V_{IF}$ in the case of eq
267 9. For evaluation of Γ , we search this grid for the values
268 immediately inferior (E_k^{n-1}) and superior (E_k^n) to E_k and
269 compute Γ with the linearly interpolated cross section

$$\sigma_{IF}(E_k) = \sigma_{IF}(E_k^{n-1}) + \frac{\sigma_{IF}(E_k^n) - \sigma_{IF}(E_k^{n-1})}{(E_k^n - E_k^{n-1})} (E_k - E_k^{n-1})$$

$$(11)$$

271 **2.3. Cross Sections.** From the light–matter interaction
272 theory up to first order and in the electric-dipole
273 approximation, it is possible to show that the state-resolved
274 photoionization cross section for this process is given by the
275 expression^{55,56}

$$\sigma_{IF}(E, E_k, \mathbf{R}) = \frac{\pi}{\epsilon_0 \hbar c} E |D_{IF}^k(\mathbf{R})|^2$$

$$(12)$$

277 where ϵ_0 is the vacuum permittivity and c is the speed of light.
278 The quantity $D_{IF}^k(\mathbf{R})$ denotes the photoelectron transition
279 dipole matrix element as a function of the nuclear coordinates
280 \mathbf{R} , formally defined as

$$D_{IF}^k(\mathbf{R}) = \langle \Phi_F^k(\mathbf{r}; \mathbf{R}) | \boldsymbol{\mu} \cdot \hat{\mathbf{e}} | \Phi_I(\mathbf{r}; \mathbf{R}) \rangle \quad (13)$$

282 where $\Phi_I(\mathbf{r}; \mathbf{R})$ and $\Phi_F^k(\mathbf{r}; \mathbf{R})$ are the corresponding electronic
283 wave functions before and after the ionization. Note that Φ_F^k
284 also describes the ejected electron with wavevector \mathbf{k} . The
285 remaining terms in eq 13 are the electric dipole operator $\boldsymbol{\mu}$ and
286 the unit vector $\hat{\mathbf{e}}$ in the direction of the electric field of the laser.
287 Integration in eq 13 is over the electronic coordinates \mathbf{r} .
288 Naturally, eq 12 implies that we are assuming a weak radiation
289 intensity regime where the perturbative approach holds.

290 Usually, the transition dipole matrix is computed within the
291 Condon approximation at the nuclear equilibrium geometry \mathbf{R}_0 .
292 The nuclear ensemble, however, is intrinsically a post-Condon
293 approach, as the transition moments are by construction
294 computed for a distribution of nuclear geometries. For this

reason, working equations are derived here implicitly retaining
the dependence of D_{IF}^k on \mathbf{R} .

Now, assuming the photoelectron ejection is fast, the final
electronic state can be represented by the uncorrelated
product³⁶

$$\Phi_F^k = \tilde{\Phi}_F \psi_F^k \quad (14)$$

ψ_F^k is the wave function of the ejected electron and $\tilde{\Phi}_F$ the
electronic wave function describing the F state of the remaining
 $N - 1$ electron species. Also assuming that ψ_F^k is orthogonal to
the orbitals of the initial state (strong orthogonality
conditions), then

$$|D_{IF}^k|^2 = |\langle \psi_F^k | \boldsymbol{\mu} \cdot \hat{\mathbf{e}} | \psi_{IF}^d \rangle_{\mathbf{r}_N}|^2 \quad (15)$$

Integration in eq 15 is over only one electron coordinate, \mathbf{r}_N in
this case. $\psi_{IF}^d(\mathbf{r}_N)$ is the Dyson orbital (DO) associated with the
particular $I \rightarrow F$ transition, formally defined as^{57,58}

$$\psi_{IF}^d(\mathbf{r}_N) = \sqrt{N} \langle \tilde{\Phi}_F | \Phi_I \rangle_{\{\mathbf{r}_{N-1}\}} \quad (16)$$

where the integration is here over the remaining $N - 1$ electron
coordinates. Note that ψ_{IF}^d is defined for a given nuclear
configuration \mathbf{R} . Introducing the norm of the Dyson orbital
 $\|\psi_{IF}^d\|$, eq 15 can be rewritten as

$$|D_{IF}^k|^2 = \|\psi_{IF}^d\|^2 |\langle \psi_F^k | \boldsymbol{\mu} \cdot \hat{\mathbf{e}} | \bar{\psi}_{IF}^d \rangle_{\mathbf{r}_N}|^2 \quad (17)$$

where $\bar{\psi}_{IF}^d = \psi_{IF}^d / \|\psi_{IF}^d\|$ is just the DO normalized to one.

Once the DOs and their norms are known, the right-hand
side of eq 17 can be evaluated. In this work, after computing the
DOs as explained later in section 2.4, we have used the EZDYSON
3.2 program^{34,36} to compute $\sigma_{IF}(\mathbf{R}_l)$. This program offers the
options of representing ψ_F^k on a basis set of Spherical or
Coulomb partial waves,⁵⁹ and also includes isotropic angular
averaging of the photoelectron dipole matrix elements. The free
electron states are represented by^{32,33}

$$\psi_F^k(\mathbf{r}) = \frac{m_e^{1/2}}{\hbar} k^{1/2} F_k(\mathbf{r}) \quad (18)$$

where $F_k(\mathbf{r})$ is the electron wave expansion in a convenient
basis and ψ_F^k is normalized to energy interval (i.e., it has units of
(volume \times energy)^{-1/2}). Thus, the transition moment is

$$|D_{IF}^k|^2 = \frac{m_e g_I}{3 \hbar^2} k \|\psi_{IF}^d\|^2 |\langle F_k | \boldsymbol{\mu} | \bar{\psi}_{IF}^d \rangle_{\mathbf{r}_N}|^2 \quad (19)$$

The factor $1/3$ stems from the isotropic averaging, while g_I
accounts for spin and orbital degeneracies of state I . Replacing
eq 19 into eq 12 renders

$$\sigma_{IF} = \frac{\pi}{3} \frac{m_e g_I}{\epsilon_0 c \hbar^3} k E \|\psi_{IF}^d\|^2 |\langle F_k | \boldsymbol{\mu} | \bar{\psi}_{IF}^d \rangle_{\mathbf{r}_N}|^2 \quad (20)$$

In addition to simulations based on the full computation of the
cross sections, we have also simulated the spectrum based on a
second approach, which consists of simply approximating eq 20
to

$$\sigma_{IF} \approx C \|\psi_{IF}^d\|^2 \quad (21)$$

where C is an arbitrary constant. In this case, all functional
dependence of the transition dipole moments on the
geometries and final states are supposed to be contained in
the DO norms.

343 In the remaining text, when using eq 20 to simulate the
344 spectrum, we will refer to it as the cross section approach, and
345 when using eq 21, it will be called the DO norm approach.

346 **2.4. Dyson Orbitals.** The DO associated with a particular I
347 $\rightarrow F$ transition (eq 16) is a single electron wave function
348 containing information on where the ejected electron was
349 removed from. According to our previous developments, once
350 the DOs are known, the cross sections can be evaluated, and
351 the photoelectron spectrum can be fully computed. In the
352 Supporting Information (SI-1), we provide a detailed
353 discussion on how to compute DOs. Here, we will outline
354 only a few key aspects.

355 As shown in the SI, eq 16 can be rewritten as a linear
356 combination of spin-orbitals χ_q as

$$\psi_{IF}^d(\mathbf{r}_N) = \sum_{s=1}^{N_{bf}} b_s \chi_s(\mathbf{r}_N) \quad (22)$$

357 with

$$b_s = \sum_{n=0}^{N_{\max}} \sum_{j=1}^N d_{nj}^q \delta_{qs} \quad (23)$$

358 where δ_{qs} is the Kronecker delta function. The coefficients

$$d_{nj}^q = (-1)^{N+j} c_n \sum_{m=0}^{M_{\max}} \tilde{c}_m \langle \tilde{\Psi}_m | \Psi_n^j \rangle \quad (24)$$

359 are computed in terms of Slater determinant overlaps $\langle \tilde{\Psi}_m | \Psi_n^j \rangle$
360 and configuration interaction (CI) coefficients c_n and \tilde{c}_m
361 defining the electronic wave functions of the N and $N-1$
362 electron systems, respectively. To reduce computational costs,
363 d_{nj}^q terms with expansion coefficient c_n or \tilde{c}_m smaller than an
364 arbitrarily small value ϵ_{cis} can be neglected. In all results
365 discussed here, we have adopted $\epsilon_{cis} = 0.01$.

366 Using eq 22, the DO norm can be easily computed as

$$\|\psi_{IF}^d\| = \left(\sum_{s=1}^{N_{bf}} b_s^2 \right)^{1/2} \quad (25)$$

367 which, in general, is not equal to 1. In fact, $\|\psi_{IF}^d\|$ may range
368 from 0 to 1 and, as can be inferred from eq 21, it is a measure of
369 the photoelectron ejection probability.⁶⁰ The closer is the norm
370 to 0 (1), the less (more) probable is the ionization.

371 While, the Slater determinant overlaps required in eq 24 can
372 be readily computed in terms of the overlap matrix between
373 atomic orbitals $S_{uv} = \langle \phi_u | \phi_v \rangle$, a standard output when
374 computing the electronic states, the CI coefficients in the
375 framework of linear-response TDDFT requires some additional
376 discussion, which is done in the next section.

377 **2.4.1. Dyson Orbitals with TDDFT.** The theory presented so
378 far in this section to compute the DOs is general and can in
379 principle be applied for any method used to solve the electronic
380 problem. The only condition is the representation of the
381 electronic wave functions as a linear combination of Slater
382 determinants. Within the frame of Hartree–Fock based
383 methods, that introduces no problem as it is a common
384 assumption of the methodology. Therefore, the expansion
385 coefficients c_n and \tilde{c}_m are directly computed. In the case of
386 TDDFT, approximated wave functions in the CI form should
387 be built.

388 According to the Casida's Ansatz for state assignment,⁶¹ the
389 electronic wave function corresponding to a given excited state
390 K can be represented as

$$\Phi_K = \sum_o \sum_v C_{ov}^K \Psi_{ov} \quad (26)$$

391 where o and v stand for occupied and virtual spin-orbitals of
392 the same spin, respectively. Denoting by Ψ_0 the Kohn–Sham
393 ground-state determinant, Ψ_{ov} are singly excited Slater
394 determinants, where the o th occupied spin-orbital has been
395 replaced by the v th virtual one of the same spin, analogous to a
396 configuration interaction with single excitations. Notice that
397 only excited Slater determinants are included in eq 26. The
398 ground state wave function is by definition $\Phi_0 = \Psi_0$.

399 The use of eq 26 for building wave functions out of TDDFT
400 amplitudes has become very popular recently.⁶² It has been
401 extensively used for computations of nonadiabatic couplings in
402 dynamics simulations^{63–66} and also employed to compute
403 different types of quantities, including spin-orbit couplings,⁶⁷
404 transition dipole moments,^{20,68} nonadiabatic coupling vectors,
405 ^{68,69} and Dyson orbitals.¹³ In fact, this same methodology
406 has been generalized⁷⁰ to build wave functions to other linear-
407 response-based methods as well, like ADC(2) and CC2.^{71–75}
408 For a critical discussion of this approximation, see refs 76 and
409 77.

410 The expansion coefficients in eq 26 can be explicitly
411 computed as⁶¹

$$C_{ov}^K = A_K (X_{ov}^K + Y_{ov}^K) \quad (27)$$

412 where $X^K + Y^K$ is the linear response TDDFT vector associated
413 with the K th electronic state and

$$A_K = \left(\sum_{o,v} |(X_{ov}^K + Y_{ov}^K)|^2 \right)^{-1/2} \quad (28)$$

414 is a normalization factor introduced to ensure electronic wave
415 functions normalized to unity. This normalization factor is
416 needed to account for the ansatz in eq 26 being well-defined
417 only for TDDFT with functionals without any fraction of
418 Hartree–Fock exchange.

3. STEADY PE SPECTRA OF IMIDAZOLE AND ADENINE

426 According to the developments of section 2.1, calculation of the
427 steady spectrum at a given value of kinetic energy E_k of the
428 photoelectron can be pictured in three main steps: (i)
429 generation of the nuclear ensemble; (ii) calculation of the
430 DOs and ionization potentials (IPs) for each nuclear
431 configuration and F electronic state considered; and (iii)
432 calculation of the individual photoelectron intensities, from
433 which the full spectrum is statistically computed. Along this
434 section, we will illustrate each of these steps when applied to
435 the He(I) photoionization of imidazole⁴⁵ and adenine.⁴⁴

436 **3.1. Nuclear Ensemble.** The steady PE spectra of
437 imidazole and adenine were computed at $E = 21.21$ eV,
438 which corresponds to the energy of a He(I) source. As the
439 ionization is assumed to occur from the electronic and
440 vibrational ground states, the nuclear configurations were
441 sampled according to eq 6. An ensemble of $N_p = 500$ nuclear
442 geometries was generated in normal modes coordinates for
443 each molecule and then transformed back to Cartesian
444 coordinates. The equilibrium geometries \mathbf{R}_0 , normal-mode
445 frequencies ω_i , and normal mode eigenvectors were computed
446

Table 1. IPs (in eV) and DO norms $\|\psi_{0F}^d\|$ Corresponding to Each $0 \rightarrow F$ Transition for the Equilibrium Geometry of Imidazole. The Experimental IPs Reported in ref 45 Are Given As Well

F	$\Delta V_{0F}^{\text{expt}}$	$\Delta V_{0F}(\mathbf{R}_0)$	$\ \psi_{0F}^d(\mathbf{R}_0)\ $	F	$\Delta V_{0F}^{\text{expt}}$	$\Delta V_{0F}(\mathbf{R}_0)$	$\ \psi_{0F}^d(\mathbf{R}_0)\ $
0	8.81	8.99	0.98	20	18.08	18.23	0.79
1	10.38	10.30	0.96	21		18.30	0.07
2		10.62	0.91	22		18.33	0.02
3	14.03	14.07	0.96	23		18.90	0.18
4		14.21	0.70	24		18.94	0.00
5		14.74	0.27	25		18.95	0.17
6	14.77	14.93	0.91	26		18.98	0.20
7	15.38	15.04	0.96	27	20.48	19.04	0.73
8		15.15	0.10	28		19.17	0.01
9		15.25	0.33	29		19.19	0.13
10		15.40	0.33	30		19.24	0.01
11		16.05	0.20	31		19.28	0.19
12		16.13	0.13	32		19.36	0.00
13		16.71	0.34	33		19.39	0.12
14		16.92	0.14	34		19.39	0.00
15		17.49	0.08	35		19.52	0.37
16		17.92	0.10	36		19.53	0.03
17		18.10	0.13	37		19.54	0.03
18		18.13	0.02	38		19.55	0.32
19		18.16	0.00	39		19.59	0.05

447 at B3LYP/aug-cc-pVTZ level. DFT and TDDFT calculations
448 here, as in rest of the paper, were all performed with GAUSSIAN
449 09.⁷⁸

450 **3.2. IPs and DOs.** For each nuclear configuration, the
451 electronic ground state of the neutral molecules was computed
452 within DFT at CAM-B3LYP/aug-cc-pVDZ level. The first 40
453 states of imidazole cation and the first 10 of adenine cation
454 were considered. All those doublet excited states were
455 computed within TDDFT with the same functional⁷⁹ and
456 basis set.⁸⁰

457 After building approximated electronic wave functions for all
458 these states, the DOs corresponding to each particular $I = 0$
459 (neutral) $\rightarrow F$ (cation) transition were computed according to
460 the formalism presented in section 2.4. To illustrate this step in
461 more details, Table 1 (imidazole) and Table 2 (adenine)
462 present the values of ΔV_{0F} and $\|\psi_{0F}^d\|$ for the corresponding
463 equilibrium geometries of each system, together with the IPs
464 for each molecule.^{44,45}

Table 2. IPs (in eV) and DO Norms $\|\psi_{0F}^d\|$ Corresponding to Each $0 \rightarrow F$ Transition for the Equilibrium Geometry of Adenine. Experimental IPs Reported in ref 44 and OVGf/6-311++G** Data from ref 49 Are Given As Well

F	$\Delta V_{0F}^{\text{expt}}$	$\Delta_{\text{TD-CAM-B3LYP}}$		OVGF ^a	
		$\Delta V_{0F}(\mathbf{R}_0)$	$\ \psi_{0F}^d(\mathbf{R}_0)\ $	$\Delta V_{0F}(\mathbf{R}_0)$	$P^{1/2}$
0	8.48	8.35	0.98	8.32	0.95
1	9.58	9.51	0.94	9.40	0.94
2		9.69	0.87	9.45	0.94
3	10.50	10.45	0.95	10.50	0.94
4		10.62	0.88	10.53	0.94
5	11.39	11.37	0.93	11.61	0.94
6	12.10	12.02	0.80	12.28	0.93
7		13.06	0.32		
8		13.24	0.11		
9	13.21	13.48	0.52	13.63	0.92

^a $P^{1/2}$ is the square root of the OVGf intensity.

As can be seen from the tables, theoretical IPs are in excellent
agreement with experimental ones. Another interesting feature
that can be appreciated is that although all $0 \rightarrow F$ transitions are
energetically allowed ($\Delta V_{0F} \leq E$), not all of them contribute to
the spectrum. For imidazole, for instance, only a few transitions
really do so, the rest being practicably negligible, given their
small DO norms. Moreover, among the significant transitions,
we can find very intense ones (norms close to one), such as the
 $0 \rightarrow 0$ in both molecules, and some much less intense, such as
the $0 \rightarrow 9$ for imidazole or $0 \rightarrow 7$ for adenine. Thus, with DO
norms alone, one can identify not only which transitions really
contribute to the spectrum, but also what the relative
contribution from each transition will be.

Table 2 also shows outer valence green function (OVGF)
results for adenine.⁴⁹ As this method is one of the most reliable
approaches for determination of IPs, they help to gauge the
quality of the current Δ_{TDDFT} results. Up to 12 eV (D_8), these
two data sets are in excellent agreement with each other, with a
RMSD of 0.2 eV for the IPs. Above 12 eV, however, the
agreement is not as good; TDDFT distributes the intensity of
the 13.21 eV experimental band over three low-intensity states
(D_7 – D_9), while OVGf still predicts a single state. The
quantitative comparison to the experiment favors TDDFT
though.

3.3. Steady PE Spectrum. Once IPs and DOs (eq 22) are
computed for each nuclear configuration \mathbf{R}_i of the ensemble
(eq 6) and for F electronic state of the cation, the spherically
averaged total cross section for the same geometries ($\sigma_{IF}(\mathbf{R}_i)$),
are computed, and the spectrum is simulated (eq 5). σ_{IF}
(\mathbf{R}_i) are computed with the EZDYSON 3.2 program. The free-
electron wave function was expanded in Coulomb partial waves
to an angular momentum of $l_{\text{max}} = 6$, which we found out to be
enough to converge the ionization probabilities. The photo-
electron dipole matrix elements were averaged over all
molecular orientations, which is justified by the nonpolarized
character of the laser used in the experiments and the random
orientation of the molecules before the ionization. Alternatively,

we have also computed the spectrum based on the DO norm approach, using eq 21.

The simulated PE spectra obtained by both approaches, cross section and DO norm, are shown in Figure 3 for imidazole and

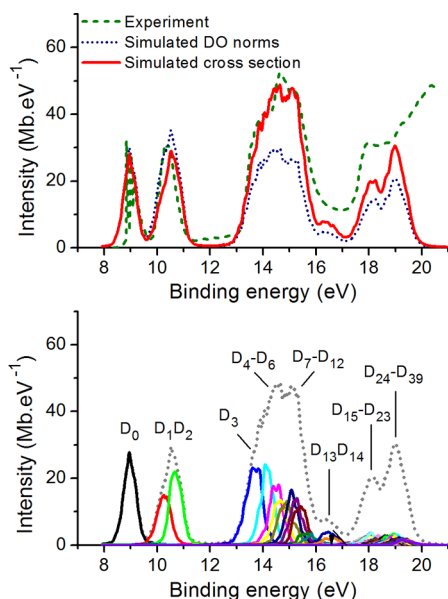


Figure 3. Simulated (this work) and experimental⁴⁵ steady PE spectra of imidazole for a laser energy of 21.21 eV. The intensities of the experimental spectrum and of the simulation based on DO norms are normalized to match the maximum of the first peak. Bottom: Individual contributions from each cationic state up to D_{39} ; the dotted line shows the sum over all components. $\epsilon = 0.1$ eV.

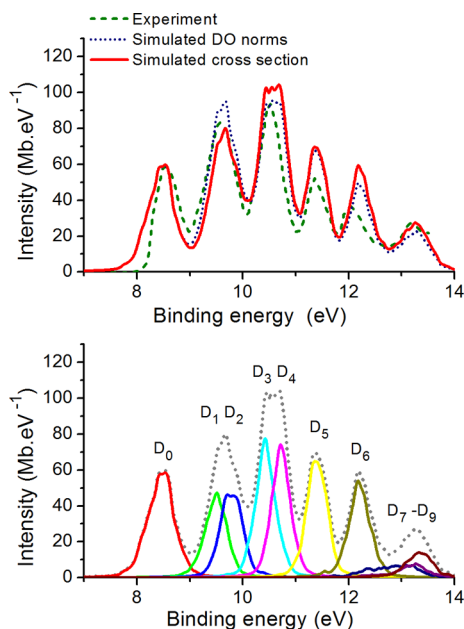


Figure 4. Top: Simulated (this work) and experimental⁴⁴ steady PE spectra of adenine for a photon energy of 21.21 eV. The intensities of the experimental spectrum and of the simulation based on DO norms are normalized to match the maximum of the first peak. Bottom: Individual contributions from each cationic state up to D_9 . The dotted line shows the sum over all components. $\epsilon = 0.1$ eV.

Figure 4 for adenine. Experimental results from refs 44 and 45 are shown as well. All curves are represented as a function of the binding energy, defined as $E_b = E - E_k$. As can be seen in the figures, the theoretical methods are able to correctly reproduce both the position and width of the bands. The relative intensity of the bands shows some dependency on the method, but a nice agreement with the experiment is in general reached. For imidazole, the DO norm approach renders the medium and high energy bands at 14 and 18 eV with too low intensities, as compared to the low energy bands. The full computation of the transition moments in the cross section approach tends to deliver better balanced relative intensities.

Concerning intensity, only the cross section approach can provide absolute values. In Figure 3 and Figure 4, the intensities of the spectra based on DO norms are normalized to match the intensity of the first peak of the spectra based on cross sections. Unfortunately, absolute intensities for these molecules have not been experimentally reported, and the same normalization procedure was applied.

The good agreement between the spectra computed with cross sections and DO norms in the low binding energy region implies that the cross section approximation in eq 21 is valid for $E \gg \Delta V_{IF}$. Thus, as long as absolute intensities are not required, the low-energy region of the photoelectron spectrum may be simulated with the DO norm approach, significantly reducing computational costs.

The bottom graphs of Figure 3 and Figure 4 show the contribution of each $S_0 \rightarrow D_n$ transition to the total cross section. For both molecules, only few cation states contribute to the spectrum up to 14 eV. In some cases, a single experimental band may correspond to the overlap of transitions into more than one state, as for instance transitions into D_1 and D_2 forming the second photoelectron band of the two molecules.

Above 14 eV, the number of states needed to compute the spectrum increases substantially. For imidazole, for instance, transitions into nine states (D_3 to D_{12}) contribute to the broad band starting at 13 eV. For the next band starting at 18 eV, even considering 24 states (D_{15} to D_{39}), we have not been able to reproduce the experimental band shape. This large demand for states in the high energy region points to a major limitation of the method. Not only the simulation costs may be prohibitive, but also the computed properties of such highly excited states are not fully reliable, especially within a linear-response approximation.⁸¹

4. TIME-RESOLVED PE SPECTRA OF IMIDAZOLE

As in the steady case, the calculation of the time-resolved PE spectrum at a given E_k can also be pictured in three main steps: (i) generation of the nuclear ensemble, (ii) computation of the DOs and IPs, and (iii) calculation of photoelectron intensities, from which the spectrum is statistically computed. However, according to the developments of section 2.2, step (i) is fundamentally different now: the nuclear ensemble has to be selected from nonadiabatic dynamics. Along this section, we illustrate all these steps, when applied to simulate the time- and kinetic-energy-resolved PE spectrum of imidazole.

4.1. Nuclear Ensemble from Surface Hopping. As imidazole is initially pumped from the vibrational ground state, the sampling of the nuclear coordinates and conjugate momenta at $t = 0$ was performed according to a Wigner distribution function for S_0 . The same \mathbf{R}_0 , ω_j , and normal-mode eigenvectors as in section 3.1 were used. A set of 500 nuclear

567 configurations and conjugate momenta were generated and
 568 projected onto the adiabatic electronic states to compute the
 569 absorption spectrum shown in Figure 5.

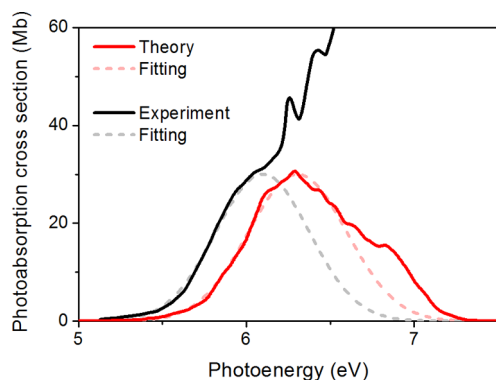


Figure 5. Simulated and experimental⁴³ absorption spectrum of imidazole in the gas phase. The intensity of the experimental spectrum was normalized to match the simulated one.

570 In the experimental setup,¹⁵ a pump laser of energy $E_1 = 6.18$
 571 eV (200.8 nm) was used to directly excite imidazole from the
 572 electronic ground state into the $^1\pi\pi^*$ state. From the
 573 computational side, using TDDFT at CAM-B3LYP/aug-cc-
 574 pVDZ level, we found out that the simulated absorption
 575 spectrum is blue-shifted by 0.2 eV compared to the
 576 experimental spectrum⁴³ (Figure 5). Therefore, to excite the
 577 $^1\pi\pi^*$ state of imidazole in the same region as done in the
 578 experiments, an energy $E_1 = 6.4$ eV is necessary in the
 579 computational modeling. This value was used in the
 580 simulations.

581 To initiate the dynamics, 500 phase-space points sampled for
 582 the absorption spectrum were screened to select those with
 583 excitation energy $E_I - E_0$ within the narrow energy interval E_1
 584 ± 0.1 eV, and resampled using their corresponding oscillator
 585 strength as transition probability.⁴ A set of 100 points matching
 586 these energy-window and oscillator-strength criteria was
 587 selected to be used as initial conditions for trajectories.

588 The number of initial conditions per adiabatic electronic
 589 state is shown in Table 3. This distribution reflects the

Table 3. Number of Initial Conditions per Electronic State for Which $E_I - E_0$ is within the Energy Interval $E_1 \pm 0.1$ eV

S_1	S_2	S_3	S_4	S_5	S_6	S_7	total
0	26	46	21	6	1	0	100

590 geometric distortions in the sampling. Although the vertical
 591 excitation into the bright $\pi\pi^*$ state is S_3 for the equilibrium
 592 geometry, Table 3 shows that, depending on the geometry, this
 593 state may shift as down as S_2 and as high as S_6 .

594 The electronic energies, energy gradients, and nonadiabatic
 595 coupling terms were computed “on-the-fly” within the frame of
 596 the TDDFT at CAM-B3LYP/aug-cc-pVDZ level. Excited
 597 electronic states up to S_8 were included in the dynamics.
 598 Each trajectory was propagated for a maximum of $t = 500$ fs,
 599 with an integration step of 0.5 fs for classical equations and
 600 0.025 fs for quantum equations.

601 Nonadiabatic transitions between different electronic states
 602 were treated with the fewest-switches surface hopping⁸²
 603 including decoherence corrections ($\alpha = 0.1$ hartree).⁸³

Nonadiabatic couplings with TDDFT were computed by finite
 differences with the method discussed in ref 63 which is based
 on the Hammes-Schiffer/Tully approach.⁸⁴ As a single-
 reference method, TDDFT cannot provide reliable non-
 adiabatic couplings for crossings with the ground state. For
 this reason, when a trajectory reached an S_1-S_0 energy gap
 smaller than 0.15 eV before the maximum simulation time, it
 was stopped. This procedure did not affect the spectrum
 simulations, as at this point the probe energy was already
 smaller than the ionization energy.

After completing the dynamics, trajectories were split in
 regular intervals of $\Delta\tau = 25$ fs starting from $\tau = 0$. For each time
 interval i between 0 and the maximum simulation time, $N_p =$
 500 nuclear geometries $\mathbf{R}_i^{(j)}$ were randomly selected from the
 trajectories and used to compute the spectrum.

Initial conditions, semiclassical dynamics, absorption spec-
 trum, and photoionization spectrum were computed with
 NEWTON-X interfaced with GAUSSIAN 09.

4.2. IPs and DOs. According to ref 15, a laser of $E_2 = 4.93$
 eV (251.6 nm) was used in the experiment to probe the
 dynamics after the $E_1 = 6.18$ eV (200.8 nm) pump excitation. In
 the simulation, for each $\mathbf{R}_i^{(j)}$, the DOs and their norms
 associated with each $I \rightarrow F$ transition were computed, where I is
 the current electronic state of the neutral molecule at the
 moment of the ionization and F is all cation states from 0 to 4.

Before proceeding with the spectrum discussion, it is
 illustrative to characterize the ionization process for the S_0
 equilibrium geometry \mathbf{R}_0 , which approximately corresponds to
 the ionization at $\tau = 0$. Excitation energies, IPs, and DO norms
 for the lowest $I \rightarrow F$ transitions are shown in Table 4. As can be
 seen, only electronic states of the cation up to $F = 2$ (D_2) need
 to be considered for this particular geometry. (In fact, this is
 also true for all remaining geometries.)

The DOs corresponding to ionizations from S_0 (closed shell)
 and S_3 ($\pi\pi^*$) are shown in Figure 6. The main configuration for
 each singlet and doublet state is schematically shown in the
 figure as well. The doublet configurations differ from that for S_0
 by a single spin orbital. Therefore, according to the ionization
 rules discussed in the Supporting Information (SI-2), such
 ionization processes are allowed. This is corroborated by the
 large DO norms for $S_0 \rightarrow D_n$ processes reported in Table 4. In
 the case of S_3 , only ionization into D_0 is allowed according to
 the ionization rules, which is also corroborated by the results in
 Table 4. As we discuss below, this ionization pattern from S_3
 will have major consequences for the simulation of the time-
 resolved spectrum.

4.3. Time-Resolved Spectrum. Once IPs and DOs are
 known for each nuclear geometry $\mathbf{R}_i^{(j)}$ between the current state
 I and F cation states, the time-resolved PE spectrum can be
 computed either with the cross section approach (eq 20) or
 with the DO norm approach (eq 21). Then, if we suppose that
 the electron is ejected with the maximum kinetic energy, the
 photoelectron spectrum is computed based on peaked line
 shapes (PVB model), as given by eq 7. In Figure 7-top the
 simulated spectrum using the PVB model is shown for the early
 dynamics, collecting configurations generated in the first 25 fs
 of dynamics simulations. The experimental spectrum from ref
 15 for zero time delay is also shown, normalized to the
 maximum of the simulated result. (For an analysis of the
 experimental results, see ref 15, 46, and 47). The spectra are
 plotted in terms of the binding energy $E_b = E_1 + E_2 - E_k$.
 Transition dipoles were computed with Coulomb partial waves
 ($l_{\max} = 6$) between the current neutral state at a certain time

Table 4. Vertical Excitation Energies (Singlet–Singlet; ΔE_{0I} in eV) and Vertical IPs (Singlet–Doublet; ΔV_{IF} in eV) Computed at the Equilibrium Geometry R_0 ^a

I/F		ΔE_{0I} (eV) [<i>f</i>]	ΔV_{IF} (eV) [$\ \psi_{IF}^d\ ^2$]		
			0	1	2
			D_0 (π_1^{hole})	D_1 (n^{hole})	D_2 (π_2^{hole})
0	S_0 (cs)	0.00	8.99 [0.96]	10.30 [0.91]	10.62 [0.83]
1	S_1 ($\pi_1 3s_N$)	5.59 [0.000]	3.40 [0.47]	4.71 [0.00]	5.02 [0.00]
2	S_2 ($\pi_1 3s_C$)	6.36 [0.030]	2.64 [0.47]	3.95 [0.00]	4.26 [0.00]
3	S_3 ($\pi_1 \pi_1^*$)	6.43 [0.169]	2.56 [0.42]	3.87 [0.00]	4.19 [0.01]
4	S_4 ($\pi_1 3s_C$)	6.63 [0.000]	2.36 [0.38]	3.67 [0.00]	3.99 [0.00]
5	S_5 ($n\pi_1^*$)	6.72 [0.004]	2.28 [0.00]	3.59 [0.31]	3.90 [0.00]
6	S_6 ($\pi_2 3s_N$)	6.99 [0.002]	2.00 [0.00]	3.31 [0.00]	3.62 [0.36]

^aThe values of the oscillator strength (*f*) and of the squared DO norm ($\|\psi_{IF}^d(R_0)\|^2$) are shown in brackets. State assignments in terms of the main orbital contribution are given in parentheses. Notation: cs, closed shell; $3s_X$, 3s Rydberg orbital on atom X.

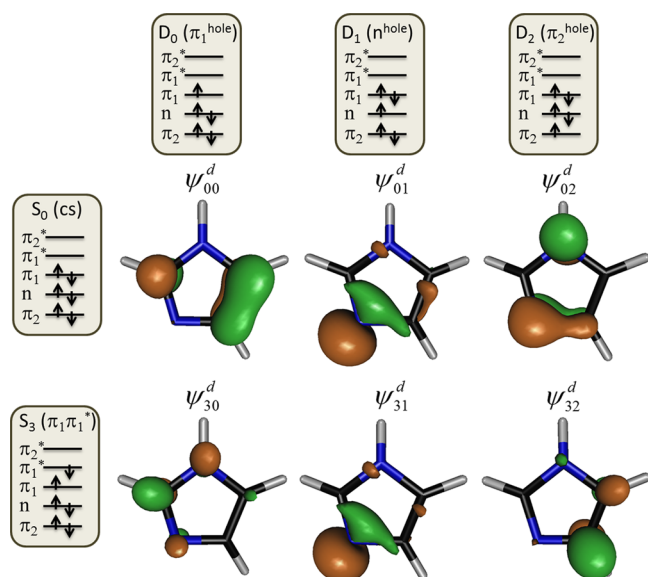


Figure 6. DOs for ionization from S_0 (closed shell) and S_3 ($\pi\pi^*$) into the first three cation states (D_0 to D_2) computed for the equilibrium geometry of imidazole with TDDFT.

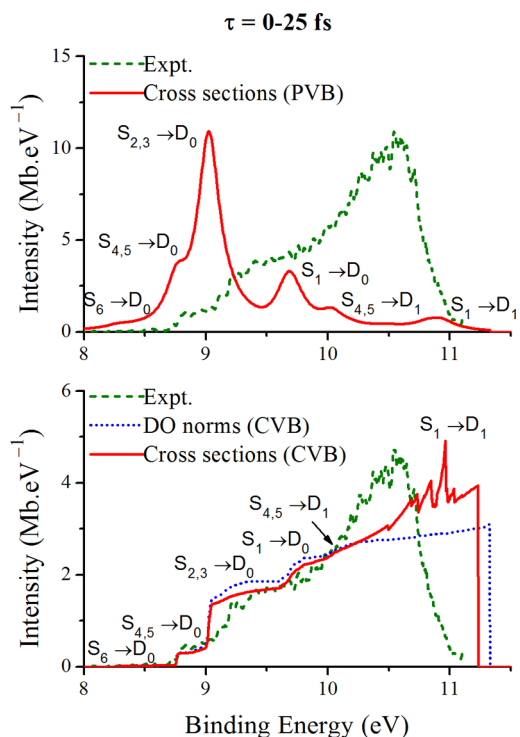


Figure 7. Photoelectron spectrum for configurations sampled within the first 25 fs of the dynamics simulations. Top: spectrum based on the PVB model. Bottom: spectrum based on the CVB model. In both cases, experimental data from ref 15 are shown. Different normalizations of experimental data are applied in each panel (see text).

667 step and all cation states up to $F = 4$ (D_3). The line width was
668 assumed to be $\varepsilon = 0.2$ eV.

669 It is clear from Figure 7-top that the spectrum computed
670 with the PVB model poorly compares to the experimental
671 result. The simulation has several peaks at the resonant points
672 defined by $E_b = E_1 + E_2 - E_{kIF}^{\text{max}} = E_1 + \Delta V_{IF}$, with the main
673 contribution coming from ionization of S_2 and S_3 into D_0 . The
674 experimental spectrum, on its turn, is much broader and it
675 peaks at much larger binding energies than predicted by the
676 simulation.

677 The large binding energy in the experimental data shown in
678 Figure 7-top implies that electrons are being ejected with low
679 kinetic energies, which has been attributed by Humeniuk et
680 al.¹³ to a rearrangement of the nuclear wavepacket due to its
681 interaction with the probe pulse. This also means that the
682 hypothesis underlying the PVB model, that is, that electrons are
683 ejected at the maximum kinetic energy, does not hold in the
684 present case and simulations based on the CVB model may be
685 more adequate. In Figure 7-bottom, we show the spectrum
686 simulated with this model, as given by eq 9, for times smaller
687 than 25 fs. As before, transition dipoles were computed with
688 Coulomb partial waves ($l_{\text{max}} = 6$) between the current neutral

state and all cation states up to $F = 4$. $n_{li} = 10$ points were used
689 in the linear interpolation of eq 11. The experimental spectrum
690 from ref 15 for zero delay is also shown, but now normalized to
691 the intensity of the $S_4 \rightarrow D_0$ contribution. 692

The agreement of the CVB model with the experiment is still
693 not perfect, but it is significantly better than with the peaked
694 model. The simulation correctly predicts a series of
695 substructures in the spectral intensity distribution. As shown
696 in Figure 7-bottom, the trace of the experimental spectrum at τ
697 = 0 exhibits inflection changes at 8.7, 9.2, and 10 eV. The
698 simulation shows equivalent inflection changes at 8.7, 9.0, and
699 9.7 eV. The data analysis revealed that they are related to which
700 neutral states are contributing to the ionization. Below 8.7 eV,
701 only ionization into D_0 coming from S_6 contributes to the
702 spectrum. Above this value, D_0 ionization of S_4 to S_5 also
703

704 contributes causing the spectral shift. Starting from 9.0 eV, the
 705 ionization of S_2 and S_3 into D_0 starts to contribute. S_1 ionization
 706 appears at above 9.7 eV. A small contribution from ionization
 707 of S_4 and S_5 into D_1 is observed above 10 eV.

708 The early dynamics spectrum computed with the DO norm
 709 approach and the CVB model is also shown in Figure 7-bottom.
 710 It is normalized to match the cross section based spectrum at
 711 the $S_4 \rightarrow D_0$ contribution. The agreement between the two
 712 approaches is very good, once more indicating that the DO
 713 norm approach can be applied as an inexpensive alternative to
 714 the full computation of the cross sections. The main difference
 715 between the two approaches is in the slope of the spectra for
 716 large binding energies. It is caused by a small effective near-
 717 linear dependence of the transition dipole on the electron
 718 kinetic energy, which is completely neglected in the DO norm
 719 approximation.

720 The time evolution of the spectrum using the CVB model
 721 with the cross section approach is shown in Figure 8. The

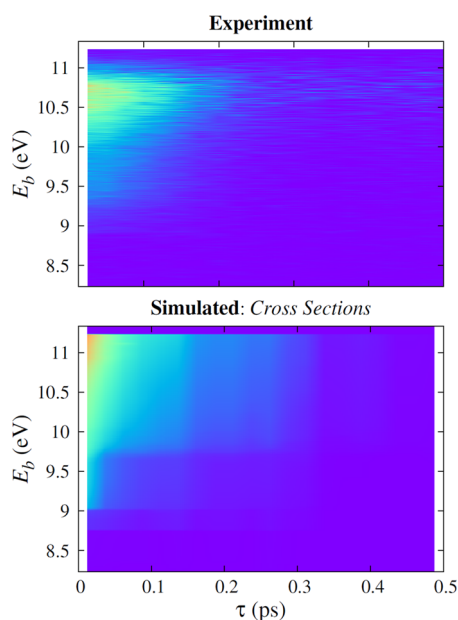


Figure 8. Time- and kinetic-energy-resolved PE spectrum of imidazole. Top: Experimental data from ref 15. Bottom: simulations using the CVB model and the cross section approach. The intensities were renormalized to match each other at $\tau = 0$ and $E_b = 9$ eV.

722 subpicosecond time distribution of the spectrum is well
 723 predicted. In particular, the simulation clearly reproduces the
 724 dependence of the time decay on the binding energy, with a
 725 systematic increase of the lifetime between 9 and 11 eV.

726 Despite the qualitative agreement between experiment and
 727 simulation with the CVB model, the predictions for the binding
 728 energy distribution are, however, not entirely satisfactory. While
 729 the experimental spectrum peaks at 10.5–10.7 eV and quickly
 730 drops to zero before the maximum binding energy (11.33 eV),
 731 the simulations do not show this important feature, but only a
 732 flat plateau extending up to the maximum binding energy (this
 733 is better seen in Figure 7-bottom). The reason underlying this
 734 difference can be traced back to three factors. First, the CVB
 735 model itself, which, as already discussed, provides only a very
 736 approximated guess on how vibrational overlaps modulate the
 737 distribution of electron kinetic energies. Second, the exper-
 738 imental setup in which electrons with small kinetic energy are
 739 not fully collected, causing the intensity drop before the

maximum binding energy. Third, a TDDFT failure to describe
 the multiconfigurational character of the $\pi\pi^*$ state of imidazole.
 This last point is discussed next.

We know from CASPT2 calculations for imidazole that the
 $\pi\pi^*$ state has strong contributions from $\pi_1\pi_1^*$ and $\pi_2\pi_2^*$
configurations (see, for instance, ref 85). This multiconfigura-
tional character plays a central role for the spectrum, splitting
the ionization signal in two components, depending on whether
the hole is created in the π_1 or π_2 orbital. The π_1^{hole} , which is
formed after ejection of the electron in the π_1^* orbital
(approximately the DO ψ_{30}^d in Figure 6), leads to an ionization
signal spanning from $E_b^{\text{min}} = \Delta V_{00} = 8.99$ eV (see Table 4) to
 $E_b^{\text{max}} = E_1 + E_2 = 11.33$ eV. On the other hand, the π_2^{hole} ,
formed after electron ejection from π_2^* (the DO ψ_{32}^d), leads to
ionization signals from $E_b^{\text{min}} = \Delta V_{02} = 10.62$ eV to again $E_b^{\text{max}} =$
11.33 eV. Thus, the sum of the two components creates a bias
toward large E_b values. TDDFT, on its turn, represents the $\pi\pi^*$
state in terms of excitations from $\pi\pi_1$ only. Therefore, only π_1
holes are created, flattening the result in the 10.5–10.7 eV
region.

5. CONCLUSIONS

We have implemented semiclassical methods based on the
nuclear ensemble approach to simulate steady and time-
resolved photoelectron spectra. The current implementation in
the NEWTON-X program works with TDDFT provided by
GAUSSIAN 09, but the methods are rather general and can be
easily adapted to work with other electronic structure levels and
programs. In section SI-3 of the Supporting Information, we
discuss the computational costs associated with these methods.

For both steady and time-resolved photoelectron spectra, we
have developed and tested two levels of approximations, one
based on full computation of transition dipole moments (cross
section approach) and another based on an approximation of
the transition dipole moments by Dyson orbital norms (DO
norm approach). Moreover, the vibrational modulation of the
electron kinetic energy distribution was also modeled with two
different approaches. In the first one, vibrational overlaps
between N and $N - 1$ electron systems were supposed to be
significant only for the electrons ejected with the maximum
allowed kinetic energy (PVB model), a common approximation
resting on the sudden-ionization hypothesis. In the second
model, vibrational overlaps were supposed to be constant over
the whole electron kinetic energy domain (CVB model).

Applications of the methods have been done for imidazole
(steady and time-resolved) and for adenine (steady). The
comparison to experimental data shows that steady spectra can
be nicely predicted with the PVB model, with good description
of intensities and band shapes.

For time-resolved spectra, the PVB model failed and the
CVB model rendered significantly better results. The CVB
simulations have been able to reproduce a series of
substructures in the spectrum, which were assigned to specific
ionization processes. Nevertheless, the overall agreement
between simulation and experiment was less satisfactory than
in the steady case due to the hypotheses underlying the CVB
model, the multiconfigurational character of the key state
contributing to the spectrum, and the instrumental signal loss
not included in the simulations. Considering all hypotheses and
approximations invoked, it is truly encouraging that the main
qualitative features of the spectrum have been predicted by the
nuclear ensemble modeling.

800 For all tested cases, the approximation of the cross sections
801 by Dyson orbital norms delivered results of similar quality as
802 those based on full computation of cross sections, with an
803 enormous economy of computational effort.

804 Finally, all these results make us confident that photoelectron
805 spectrum simulations based on the nuclear ensemble approach
806 can be an effective tool to aid deconvolution and assignment of
807 experimental data for large molecules.

808 ■ ASSOCIATED CONTENT

809 ● Supporting Information

810 The Supporting Information is available free of charge on the
811 ACS Publications website at DOI: 10.1021/acs.jctc.6b00704.

812 Full derivation of Dyson orbital formula; discussion of
813 qualitative ionization rules; estimate of computational
814 times (PDF)

815 ■ AUTHOR INFORMATION

816 Corresponding Author

817 *E-mail: mario.barbatti@univ-amu.fr.

818 Funding

819 M.B. thanks the support of the A*MIDEX grant (No. ANR-11-
820 IDEX-0001-02) funded by the French Government «Investis-
821 ssements d'Avenir» program. This work was granted access
822 to the HPC resources of Aix-Marseille Université financed by
823 the project Equip@Meso (ANR-10-EQPX-29-01) also within
824 the program «Investissements d'Avenir» supervised by the
825 Agence Nationale de la Recherche.

826 Notes

827 The authors declare no competing financial interest.

828 ■ ACKNOWLEDGMENTS

829 The authors thank C. Angeli and S. Ullrich for discussions.

830 ■ REFERENCES

- 831 (1) Barbatti, M.; Granucci, G.; Ruckebauer, M.; Plasser, F.; Crespo-
832 Otero, R.; Pittner, J.; Persico, M.; Lischka, H. *NEWTON-X: A package*
833 *for Newtonian dynamics close to the crossing seam*. www.newtonx.org
834 (accessed September 1, 2016). 2013.
- 835 (2) Barbatti, M.; Ruckebauer, M.; Plasser, F.; Pittner, J.; Granucci,
836 G.; Persico, M.; Lischka, H. *Newton-X: A Surface-Hopping Program*
837 *for Nonadiabatic Molecular Dynamics*. *WIREs: Comp. Mol. Sci.* **2014**,
838 *4*, 26–33.
- 839 (3) Crespo-Otero, R.; Barbatti, M. *Spectrum Simulation and*
840 *Decomposition with Nuclear Ensemble: Formal Derivation and*
841 *Application to Benzene, Furan and 2-Phenylfuran*. *Theor. Chem. Acc.*
842 **2012**, *131*, 1237.
- 843 (4) Barbatti, M.; Sen, K. *Effects of different initial condition*
844 *samplings on photodynamics and spectrum of pyrrole*. *Int. J. Quantum*
845 *Chem.* **2016**, *116*, 762–771.
- 846 (5) Kubo, R. *A Stochastic Theory of Line Shape*. In *Adv. Chem.*
847 *Phys.*. Shuler, K. E., Ed.; John Wiley & Sons, Inc.: 1969; Vol. 15, pp
848 101–127.
- 849 (6) Bergsma, J. P.; Berens, P. H.; Wilson, K. R.; Fredkin, D. R.;
850 Heller, E. J. *Electronic-Spectra from Molecular-Dynamics - a Simple*
851 *Approach*. *J. Phys. Chem.* **1984**, *88*, 612–619.
- 852 (7) Bennett, K.; Kowalewski, M.; Mukamel, S. *Probing electronic and*
853 *vibrational dynamics in molecules by time-resolved photoelectron,*
854 *Auger-electron, and X-ray photon scattering spectroscopy*. *Faraday*
855 *Discuss.* **2015**, *177*, 405–428.
- 856 (8) Petit, A. S.; Subotnik, J. E. *Appraisal of Surface Hopping as a*
857 *Tool for Modeling Condensed Phase Linear Absorption Spectra*. *J.*
858 *Chem. Theory Comput.* **2015**, *11*, 4328–4341.

- (9) Klaffki, N.; Weingart, O.; Garavelli, M.; Spohr, E. *Sampling*
859 *excited state dynamics: influence of HOOP mode excitations in a*
860 *retinal model*. *Phys. Chem. Chem. Phys.* **2012**, *14*, 14299–14305.
861
- (10) Rivalta, I.; Nenov, A.; Cerullo, G.; Mukamel, S.; Garavelli, M. *Ab*
862 *initio simulations of two-dimensional electronic spectra: The SOS//*
863 *QM/MM approach*. *Int. J. Quantum Chem.* **2014**, *114*, 85–93.
864
- (11) Polli, D.; Altoe, P.; Weingart, O.; Spillane, K. M.; Manzoni, C.;
865 Brida, D.; Tomasello, G.; Orlandi, G.; Kukura, P.; Mathies, R. A.;
866 Garavelli, M.; Cerullo, G. *Conical intersection dynamics of the primary*
867 *photoisomerization event in vision*. *Nature* **2010**, *467*, 440–443.
868
- (12) Ruckebauer, M.; Mai, S.; Marquetand, P.; González, L.
869 *Photoelectron spectra of 2-thiouracil, 4-thiouracil, and 2,4-dithiouracil*.
870 *J. Chem. Phys.* **2016**, *144*, 074303.
871
- (13) Humeniuk, A.; Wohlgemuth, M.; Suzuki, T.; Mitrić, R. *Time-*
872 *resolved photoelectron imaging spectra from non-adiabatic molecular*
873 *dynamics simulations*. *J. Chem. Phys.* **2013**, *139*, 134104.
874
- (14) Hudock, H. R.; Martínez, T. J. *Excited-State Dynamics of*
875 *Cytosine Reveal Multiple Intrinsic Subpicosecond Pathways*. *Chem-*
876 *PhysChem* **2008**, *9*, 2486–2490.
877
- (15) Crespo-Otero, R.; Barbatti, M.; Yu, H.; Evans, N. L.; Ullrich, S.
878 *Ultrafast Dynamics of UV-Excited Imidazole*. *ChemPhysChem* **2011**,
879 *12*, 3365–3375.
880
- (16) Mori, T.; Glover, W. J.; Schuurman, M. S.; Martinez, T. J. *Role*
881 *of Rydberg States in the Photochemical Dynamics of Ethylene*. *J. Phys.*
882 *Chem. A* **2012**, *116*, 2808–2818.
883
- (17) Thompson, A. L.; Martinez, T. J. *Time-resolved photoelectron*
884 *spectroscopy from first principles: Excited state dynamics of benzene*.
885 *Faraday Discuss.* **2011**, *150*, 293–311.
886
- (18) McFarland, B. K.; Farrell, J. P.; Miyabe, S.; Tarantelli, F.;
887 Aguilar, A.; Berrah, N.; Bostedt, C.; Bozek, J. D.; Bucksbaum, P. H.;
888 Castagna, J. C.; Coffee, R. N.; Cryan, J. P.; Fang, L.; Feifel, R.; Gaffney,
889 K. J.; Glowina, J. M.; Martinez, T. J.; Mucke, M.; Murphy, B.; Natan,
890 A.; Osipov, T.; Petrović, V. S.; Schorb, S.; Schultz, T.; Spector, L. S.;
891 Swiggers, M.; Tenney, I.; Wang, S.; White, J. L.; White, W.; Gühr, M.
892 *Ultrafast X-ray Auger probing of photoexcited molecular dynamics*.
893 *Nat. Commun.* **2014**, *5*, 4235.
894
- (19) Fujii, T.; Suzuki, Y.-I.; Horio, T.; Suzuki, T.; Mitric, R.; Werner,
895 U.; Bonacic-Koutecky, V. *Ultrafast photodynamics of furan*. *J. Chem.*
896 *Phys.* **2010**, *133*, 234303–9.
897
- (20) Mitrić, R.; Petersen, J.; Wohlgemuth, M.; Werner, U.; Bonačić-
898 *Koutecký, V.; Wöste, L.; Jortner, J. Time-Resolved Femtosecond*
899 *Photoelectron Spectroscopy by Field-Induced Surface Hopping*. *J.*
900 *Phys. Chem. A* **2011**, *115*, 3755–3765.
901
- (21) Stanzel, J.; Neeb, M.; Eberhardt, W.; Lisinetskaya, P. G.;
902 Petersen, J.; Mitrić, R. *Switching from molecular to bulklike dynamics*
903 *in electronic relaxation of a small gold cluster*. *Phys. Rev. A: At, Mol,*
904 *Opt. Phys.* **2012**, *85*, 013201.
905
- (22) Buchner, F.; Nakayama, A.; Yamazaki, S.; Ritze, H.-H.; Lübcke,
906 A. *Excited-State Relaxation of Hydrated Thymine and Thymidine*
907 *Measured by Liquid-Jet Photoelectron Spectroscopy: Experiment and*
908 *Simulation*. *J. Am. Chem. Soc.* **2015**, *137*, 2931–2938.
909
- (23) Wolf, T. J. A.; Kuhlman, T. S.; Schalk, O.; Martinez, T. J.;
910 Moller, K. B.; Stolow, A.; Unterreiner, A. N. *Hexamethylcyclopenta-*
911 *diene: time-resolved photoelectron spectroscopy and ab initio multiple*
912 *spawning simulations*. *Phys. Chem. Chem. Phys.* **2014**, *16*, 11770–
913 11779.
914
- (24) Tomasello, G.; Humeniuk, A.; Mitrić, R. *Exploring Ultrafast*
915 *Dynamics of Pyrazine by Time-Resolved Photoelectron Imaging*. *J.*
916 *Phys. Chem. A* **2014**, *118*, 8437–8445.
917
- (25) Cederbaum, L. S.; Domcke, W.; Schirmer, J.; Niessen, W. v.
918 *Many-Body Effects in Valence and Core Photoionization of Molecules*.
919 *Phys. Scr.* **1980**, *21*, 481.
920
- (26) Ortiz, J. V. *A nondiagonal, renormalized extension of partial*
921 *third-order quasiparticle theory: Comparisons for closed-shell*
922 *ionization energies*. *J. Chem. Phys.* **1998**, *108*, 1008–1014.
923
- (27) Herman, M. F.; Freed, K. F.; Yeager, D. L. *Analysis and*
924 *Evaluation of Ionization Potentials, Electron Affinities, and Excitation*
925 *Energies by the Equations of Motion—Green's Function Method*.
926 *Adv. Chem. Phys.* **1981**, *48*, 1–69.
927

- 928 (28) von Niessen, W.; Schirmer, J.; Cederbaum, L. S. Computational
929 methods for the one-particle green's function. *Comput. Phys. Rep.*
930 **1984**, *1*, 57–125.
- 931 (29) Nguyen, N. L.; Borghi, G.; Ferretti, A.; Dabo, I.; Marzari, N.
932 First-Principles Photoemission Spectroscopy and Orbital Tomography
933 in Molecules from Koopmans-Compliant Functionals. *Phys. Rev. Lett.*
934 **2015**, *114*, 166405.
- 935 (30) Guest, M. F.; Saunders, V. R. The calculation of valence shell
936 ionization potentials by the ϵ -SCF method. *Mol. Phys.* **1975**, *29*,
937 873–884.
- 938 (31) Barbatti, M.; Ullrich, S. Ionization potentials of adenine along
939 the internal conversion pathways. *Phys. Chem. Chem. Phys.* **2011**, *13*,
940 15492–15500.
- 941 (32) Starace, A. Photoionization of Atoms. In *Springer Handbook of*
942 *Atomic, Molecular, and Optical Physics*; Drake, G., Ed.; Springer New
943 York: New York, NY, 2006; pp 379–390.
- 944 (33) Bethe, H. A.; Salpeter, E. E. *Quantum Mechanics of One- and*
945 *Two-Electron Atoms*; Springer-Verlag: Berlin, 1957.
- 946 (34) Oana, C. M.; Krylov, A. I. Cross sections and photoelectron
947 angular distributions in photodetachment from negative ions using
948 equation-of-motion coupled-cluster Dyson orbitals. *J. Chem. Phys.*
949 **2009**, *131*, 124114.
- 950 (35) Frolov, M. V.; Manakov, N. L.; Marmo, S. S.; Starace, A. F.
951 Photodetachment of a model molecular system by an elliptically
952 polarized field. *J. Mod. Opt.* **2015**, *62*, S21–S33.
- 953 (36) Oana, C. M.; Krylov, A. I. Dyson orbitals for ionization from the
954 ground and electronically excited states within equation-of-motion
955 coupled-cluster formalism: Theory, implementation, and examples. *J.*
956 *Chem. Phys.* **2007**, *127*, 234106.
- 957 (37) Seel, M.; Domcke, W. Femtosecond time-resolved ionization
958 spectroscopy of ultrafast internal-conversion dynamics in polyatomic
959 molecules: Theory and computational studies. *J. Chem. Phys.* **1991**, *95*,
960 7806–7822.
- 961 (38) Cederbaum, L. S.; Domcke, W.; Schirmer, J.; Niessen, W. V.
962 Correlation Effects in the Ionization of Molecules: Breakdown of the
963 Molecular Orbital Picture. In *Advances in Chemical Physics*; John Wiley
964 & Sons, Inc.: 1986; pp 115–159.
- 965 (39) Seel, M.; Domcke, W. Model studies on femtosecond time-
966 resolved ionization spectroscopy of excited-state vibrational dynamics
967 and vibronic coupling. *Chem. Phys.* **1991**, *151*, 59–72.
- 968 (40) Stolow, A.; Underwood, J. G., Time-Resolved Photoelectron
969 Spectroscopy of Nonadiabatic Dynamics in Polyatomic Molecules. In
970 *Advances in Chemical Physics*; John Wiley & Sons, Inc.: 2008; pp 497–
971 584.
- 972 (41) Zaytseva, I. L.; Trofimov, A. B.; Schirmer, J.; Plekan, O.; Feyer,
973 V.; Richter, R.; Coreno, M.; Prince, K. C. Theoretical and
974 Experimental Study of Valence-Shell Ionization Spectra of Guanine.
975 *J. Phys. Chem. A* **2009**, *113*, 15142–15149.
- 976 (42) Trofimov, A. B.; Zaitseva, I. L.; Moskovskaya, T. E.;
977 Vitkovskaya, N. M. Theoretical investigation of photoelectron spectra
978 of furan, pyrrole, thiophene, and selenole. *Chem. Heterocycl. Compd.*
979 **2008**, *44*, 1101–1112.
- 980 (43) Devine, A. L.; Cronin, B.; Nix, M. G. D.; Ashfold, M. N. R. High
981 resolution photofragment translational spectroscopy studies of the
982 near ultraviolet photolysis of imidazole. *J. Chem. Phys.* **2006**, *125*,
983 184302.
- 984 (44) Peng, S.; Padva, A.; LeBreton, P. R. Ultraviolet photoelectron
985 studies of biological purines: the valence electronic structure of
986 adenine. *Proc. Natl. Acad. Sci. U. S. A.* **1976**, *73*, 2966–2968.
- 987 (45) Klasinc, L.; Ruščič, B.; Kajfež, F.; Šunjić, V. Photoelectron
988 spectroscopy of the heterocycles imidazole and methylimidazoles. *Int.*
989 *J. Quantum Chem.* **1978**, *14*, 367–371.
- 990 (46) Montero, R.; Conde, Á. P.; Ovejas, V.; Fernández-Fernández,
991 M.; Castaño, F.; Longarte, A. Ultrafast Evolution of Imidazole after
992 Electronic Excitation. *J. Phys. Chem. A* **2012**, *116*, 10752–10758.
- 993 (47) Roberts, G. M.; Stavros, V. G. The role of $\pi\sigma^*$ states in the
994 photochemistry of heteroaromatic biomolecules and their subunits:
995 insights from gas-phase femtosecond spectroscopy. *Chem. Sci.* **2014**, *5*,
996 1698–1722.
- (48) Yu, H.; Evans, N. L.; Stavros, V. G.; Ullrich, S. Investigation of 997
multiple electronic excited state relaxation pathways following 200 nm 998
photolysis of gas-phase imidazole. *Phys. Chem. Chem. Phys.* **2012**, *14*, 999
6266–6272. 1000
- (49) Trofimov, A. B.; Schirmer, J.; Kobychov, V. B.; Potts, A. W.; 1001
Holland, D. M. P.; Karlsson, L. Photoelectron spectra of the 1002
nucleobases cytosine, thymine and adenine. *J. Phys. B: At., Mol. Opt.* 1003
Phys. **2006**, *39*, 305. 1004
- (50) Lin, J.; Yu, C.; Peng, S.; Akiyama, I.; Li, K.; Lee, L. K.; LeBreton, 1005
P. R. Ultraviolet photoelectron studies of the ground-state electronic 1006
structure and gas-phase tautomerism of purine and adenine. *J. Am.* 1007
Chem. Soc. **1980**, *102*, 4627–4631. 1008
- (51) Roca-Sanjuán, D.; Rubio, M.; Merchán, M.; Serrano-Andrés, L. 1009
Ab initio determination of the ionization potentials of DNA and RNA 1010
nucleobases. *J. Chem. Phys.* **2006**, *125*, 084302. 1011
- (52) Barbatti, M.; Lischka, H.; Salzmann, S.; Marian, C. M. UV 1012
excitation and radiationless deactivation of imidazole. *J. Chem. Phys.* 1013
2009, *130*, 034305. 1014
- (53) Case, W. B. Wigner functions and Weyl transforms for 1015
pedestrians. *Am. J. Phys.* **2008**, *76*, 937–946. 1016
- (54) Barbatti, M. Nonadiabatic Dynamics with Trajectory Surface 1017
Hopping Method. *WIREs: Comp. Mol. Sci.* **2011**, *1*, 620–633. 1018
- (55) Schinke, R. *Photodissociation Dynamics: Spectroscopy and* 1019
Fragmentation of Small Polyatomic Molecules; Cambridge University 1020
Press: Cambridge, 1995. 1021
- (56) Sakurai, J. J. *Modern Quantum Mechanics*; Addison-Wesley: MA, 1022
1994. 1023
- (57) Morini, F.; Hajgató, B.; Deleuze, M. S.; Ning, C. G.; Deng, J. K. 1024
Benchmark Dyson Orbital Study of the Ionization Spectrum and 1025
Electron Momentum Distributions of Ethanol in Conformational 1026
Equilibrium. *J. Phys. Chem. A* **2008**, *112*, 9083–9096. 1027
- (58) Chong, D. P.; Gritsenko, O. V.; Baerends, E. J. Interpretation of 1028
the Kohn–Sham orbital energies as approximate vertical ionization 1029
potentials. *J. Chem. Phys.* **2002**, *116*, 1760–1772. 1030
- (59) Gozem, S.; Gunina, A. O.; Ichino, T.; Osborn, D. L.; Stanton, J. 1031
F.; Krylov, A. I. Photoelectron Wave Function in Photoionization: 1032
Plane Wave or Coulomb Wave? *J. Phys. Chem. Lett.* **2015**, *6*, 4532– 1033
4540. 1034
- (60) Ortiz, J. V. Electron Propagator Theory of the Photoelectron 1035
Spectrum of Methanesulfenic Acid. *J. Phys. Chem. A* **2000**, *104*, 1036
11433–11438. 1037
- (61) Casida, M. Time-dependent density functional response theory 1038
for molecules. In *Recent Advances in Density Functional Methods, Part I*; 1039
Chong, D., Ed.; World Scientific: Singapore, 1995; pp 155–192. 1040
- (62) Barbatti, M.; Crespo-Otero, R. Surface Hopping Dynamics with 1041
DFT Excited States. *Top. Curr. Chem.* **2014**, *368*, 415–444. 1042
- (63) Barbatti, M.; Pittner, J.; Pederzoli, M.; Werner, U.; Mitrić, R.; 1043
Bonačić-Koutecký, V.; Lischka, H. Non-Adiabatic Dynamics of 1044
Pyrrole: Dependence of Deactivation Mechanisms on the Excitation 1045
Energy. *Chem. Phys.* **2010**, *375*, 26–34. 1046
- (64) Mališ, M.; Loquais, Y.; Gloaguen, E.; Biswal, H. S.; Piuze, F.; 1047
Tardivel, B.; Brenner, V.; Broquier, M.; Juvet, C.; Mons, M.; Došlić, 1048
N.; Ljubić, I. Unraveling the Mechanisms of Nonradiative Deactivation 1049
in Model Peptides Following Photoexcitation of a Phenylalanine 1050
Residue. *J. Am. Chem. Soc.* **2012**, *134*, 20340–20351. 1051
- (65) Werner, U.; Mitrić, R.; Suzuki, T.; Bonačić-Koutecký, V. 1052
Nonadiabatic dynamics within the time dependent density functional 1053
theory: Ultrafast photodynamics in pyrazine. *Chem. Phys.* **2008**, *349*, 1054
319–324. 1055
- (66) Tapavicza, E.; Tavernelli, I.; Rothlisberger, U. Trajectory surface 1056
hopping within linear response time-dependent density-functional 1057
theory. *Phys. Rev. Lett.* **2007**, *98*, 023001–4. 1058
- (67) Franco de Carvalho, F.; Curchod, B. F. E.; Penfold, T. J.; 1059
Tavernelli, I. Derivation of spin-orbit couplings in collinear linear- 1060
response TDDFT: A rigorous formulation. *J. Chem. Phys.* **2014**, *140*, 1061
144103. 1062
- (68) Tavernelli, I.; Curchod, B. F. E.; Laktionov, A.; Rothlisberger, U. 1063
Nonadiabatic coupling vectors for excited states within time- 1064

- 1065 dependent density functional theory in the Tamm–Dancoff
1066 approximation and beyond. *J. Chem. Phys.* **2010**, *133*, 194104.
- 1067 (69) Tavernelli, L.; Tapavicza, E.; Rothlisberger, U. Nonadiabatic
1068 coupling vectors within linear response time-dependent density
1069 functional theory. *J. Chem. Phys.* **2009**, *130*, 124107.
- 1070 (70) Plasser, F.; Crespo-Otero, R.; Pederzoli, M.; Pittner, J.; Lischka,
1071 H.; Barbatti, M. Surface Hopping Dynamics with Correlated Single-
1072 Reference Methods: 9H-Adenine as a Case Study. *J. Chem. Theory*
1073 *Comput.* **2014**, *10*, 1395–1405.
- 1074 (71) Christiansen, O.; Koch, H.; Jorgensen, P. The 2nd-Order
1075 Approximate Coupled-Cluster Singles and Doubles Model CC2.
1076 *Chem. Phys. Lett.* **1995**, *243*, 409–418.
- 1077 (72) Hättig, C.; Weigend, F. CC2 Excitation Energy Calculations on
1078 Large Molecules Using the Resolution of the Identity Approximation.
1079 *J. Chem. Phys.* **2000**, *113*, 5154–5161.
- 1080 (73) Hättig, C.; Köhn, A. Transition Moments and Excited-State
1081 First-Order Properties in the Coupled-Cluster Model CC2 Using the
1082 Resolution-of-the-Identity Approximation. *J. Chem. Phys.* **2002**, *117*,
1083 6939–6951.
- 1084 (74) Schirmer, J. Beyond the Random-Phase Approximation: A New
1085 Approximation Scheme for the Polarization Propagator. *Phys. Rev. A*:
1086 *At., Mol., Opt. Phys.* **1982**, *26*, 2395–2416.
- 1087 (75) Trofimov, A. B.; Schirmer, J. An Efficient Polarization
1088 Propagator Approach to Valence Electron Excitation Spectra. *J. Phys.*
1089 *B: At., Mol. Opt. Phys.* **1995**, *28*, 2299–2324.
- 1090 (76) Li, Z.; Suo, B.; Liu, W. First order nonadiabatic coupling matrix
1091 elements between excited states: Implementation and application at
1092 the TD-DFT and pp-TDA levels. *J. Chem. Phys.* **2014**, *141*, 244105.
- 1093 (77) Ou, Q.; Bellchambers, G. D.; Furche, F.; Subotnik, J. E. First-
1094 order derivative couplings between excited states from adiabatic
1095 TDDFT response theory. *J. Chem. Phys.* **2015**, *142*, 064114.
- 1096 (78) Frisch, M. J.; Trucks, G. W.; Schlegel, H. B.; Scuseria, G. E.;
1097 Robb, M. A.; Cheeseman, J. R.; Scalmani, G.; Barone, V.; Mennucci,
1098 B.; Petersson, G. A.; Nakatsuji, H.; Caricato, M.; Li, X.; Hratchian, H.
1099 P.; Izmaylov, A. F.; Bloino, J.; Zheng, G.; Sonnenberg, J. L.; Hada, M.;
1100 Ehara, M.; Toyota, K.; Fukuda, R.; Hasegawa, J.; Ishida, M.; Nakajima,
1101 T.; Honda, Y.; Kitao, O.; Nakai, H.; Vreven, T.; Montgomery, J., J. A.;
1102 Peralta, J. E.; Ogliaro, F.; Bearpark, M.; Heyd, J. J.; Brothers, E.; Kudin,
1103 K. N.; Staroverov, V. N.; Kobayashi, R.; Normand, J.; Raghavachari, K.;
1104 Rendell, A.; Burant, J. C.; Iyengar, S. S.; Tomasi, J.; Cossi, M.; Rega,
1105 N.; Millam, N. J.; Klene, M.; Knox, J. E.; Cross, J. B.; Bakken, V.;
1106 Adamo, C.; Jaramillo, J.; Gomperts, R.; Stratmann, R. E.; Yazyev, O.;
1107 Austin, A. J.; Cammi, R.; Pomelli, C.; Ochterski, J. W.; Martin, R. L.;
1108 Morokuma, K.; Zakrzewski, V. G.; Voth, G. A.; Salvador, P.;
1109 Dannenberg, J. J.; Dapprich, S.; Daniels, A. D.; Farkas, Ö.;
1110 Foresman, J. B.; Ortiz, J. V.; Cioslowski, J.; Fox, D. J., *Gaussian 09*,
1111 revision D.01; Gaussian, Inc.: Wallingford CT, 2013.
- 1112 (79) Yanai, T.; Tew, D. P.; Handy, N. C. A New Hybrid Exchange-
1113 Correlation Functional Using the Coulomb-Attenuating Method
1114 (CAM-B3LYP). *Chem. Phys. Lett.* **2004**, *393*, 51–57.
- 1115 (80) Dunning, T. H., Jr. Gaussian Basis Sets for Use in Correlated
1116 Molecular Calculations. I. The Atoms Boron Through Neon and
1117 Hydrogen. *J. Chem. Phys.* **1989**, *90*, 1007–1023.
- 1118 (81) Casida, M. E.; Huix-Rotllant, M. Progress in Time-Dependent
1119 Density-Functional Theory. *Annu. Rev. Phys. Chem.* **2012**, *63*, 287–
1120 323.
- 1121 (82) Tully, J. C. Molecular-Dynamics with Electronic-Transitions. *J.*
1122 *Chem. Phys.* **1990**, *93*, 1061–1071.
- 1123 (83) Granucci, G.; Persico, M. Critical Appraisal of the Fewest
1124 Switches Algorithm for Surface Hopping. *J. Chem. Phys.* **2007**, *126*,
1125 134114–11.
- 1126 (84) Hammes-Schiffer, S.; Tully, J. C. Proton-Transfer in Solution -
1127 Molecular-Dynamics with Quantum Transitions. *J. Chem. Phys.* **1994**,
1128 *101*, 4657–4667.
- 1129 (85) Serrano-Andrés, L.; Fülcher, M. P.; Roos, B. O.; Merchán, M.
1130 Theoretical study of the electronic spectrum of imidazole. *J. Phys.*
1131 *Chem.* **1996**, *100*, 6484–6491.